Origin of the chiral charge density wave in transition-metal dichalcogenide

Kwangrae Kim[1,8], Hyun-Woo J. Kim[1,2,8], Seunghyeok Ha[1,8], Hoon Kim[1], Jin-Kwang Kim[1], Jaehwon Kim[1], Junyoung Kwon[1], Jihoon Seol[1], Saegyeol Jung[3,4], Changyoung Kim[3,4], Daisuke Ishikawa[5], Taishun Manjo[5], Hiroshi Fukui[5], Alfred Q. R. Baron[5], Ahmet Alatas[2], Ayman Said[2], Michael Merz[6,7], Matthieu Le Tacon[6], Jin Mo Bok[1] ✉, Ki-Seok Kim[1] ✉ & B. J. Kim[1] ✉

Chirality refers to a structure that lacks mirror symmetry. It can be observed in a wide range of platforms, from subatomic particles and molecules to living organisms. However, the underlying mechanisms that give rise to chirality in condensed matter systems have been a subject of considerable interest. Here we elucidate the mechanism of chiral charge density wave formation in the transition-metal dichalcogenide 1T-$TiSe_2$. Based on symmetry analysis, we demonstrate that charge density modulations and ionic displacements follow distinct irreducible representations of the space group, despite exhibiting similar wave vectors and a strong coupling. This charge-lattice symmetry frustration induces lattice distortions that further break all symmetries that are not common to both sectors. This ultimately gives rise to chirality. Our theory is verified using Raman spectroscopy and inelastic X-ray scattering.

In quantum solids, chirality is defined by the absence of inversion centres, roto-inversion axes and mirror/glide planes in their space group (SG) symmetries. Chirality endows electrons with diverse exotic physical properties, such as circular photogalvanic effect[1], giant anomalous Hall effect[2], non-reciprocal transport[3] and chiral anomaly[4,5], with potential applications to spintronic devices and energy harvesting technology. However, the mechanism by which chirality emerges from the constituent microscopic degrees of freedom remains unknown, and our inability to predict chiral electronic phases from the first principles severely limits the ability to fully exploit their potentially useful properties.

The proposal that chirality can arise from a multicomponent charge density wave (CDW) has opened a new avenue to explore chiral properties of quantum matters[6,7]. Experimental evidence for chiral CDWs is found from transition-metal dichalcogenides of chemical formula AB_2 (A = Ti, Ta, V and B = S, Se)[6,8–11] and kagome materials AV_3Sb_5 (A = K, Rb, Cs)[12–14], both of which support triple-$\mathbf{q}$ CDWs. Despite the fact that a CDW is an electronic order of scalar quantity, the presence of three propagation vectors ($\mathbf{q}_1$, $\mathbf{q}_2$, $\mathbf{q}_3$) allows for chirality; for example, a descriptor of chirality is given by the pseudoscalar $\mathbf{q}_1 \cdot \mathbf{q}_2 \times \mathbf{q}_3$. Scanning tunnelling microscopy of these materials exhibit different charge modulation intensities measured along three equivalent crystallographic directions, the largest (smallest) of which is defined to be $\mathbf{q}_1$ ($\mathbf{q}_3$), with which a chiral charge density can be constructed[6].

A major argument against chirality, however, is based on the fact that no evidence for a lattice symmetry breaking consistent with the putative chiral CDW phase has ever been found[15–18]. More puzzling is the recent observation of circular photogalvanic effect in 1T-$TiSe_2$, a macroscopic manifestation of chirality, which is forbidden in its known crystal structure[19]; Neumann's principle states

[1]Department of Physics, Pohang University of Science and Technology, Pohang, South Korea. [2]Advanced Photon Source, Argonne National Laboratory, Lemont, IL, USA. [3]Center for Correlated Electron Systems, Institute for Basic Science, Seoul, South Korea. [4]Department of Physics and Astronomy, Seoul National University, Seoul, South Korea. [5]Japan Synchrotron Radiation Research Institute, Sayo, Japan. [6]Institute for Quantum Materials and Technologies, Karlsruhe Institute of Technology, Karlsruhe, Germany. [7]Karlsruhe Nano Micro Facility, Karlsruhe Institute of Technology, Karlsruhe, Germany. [8]These authors contributed equally: Kwangrae Kim, Hyun-Woo J. Kim, Seunghyeok Ha. ✉e-mail: jinmobok@postech.ac.kr; tkfkd@postech.ac.kr; bjkim6@postech.ac.kr

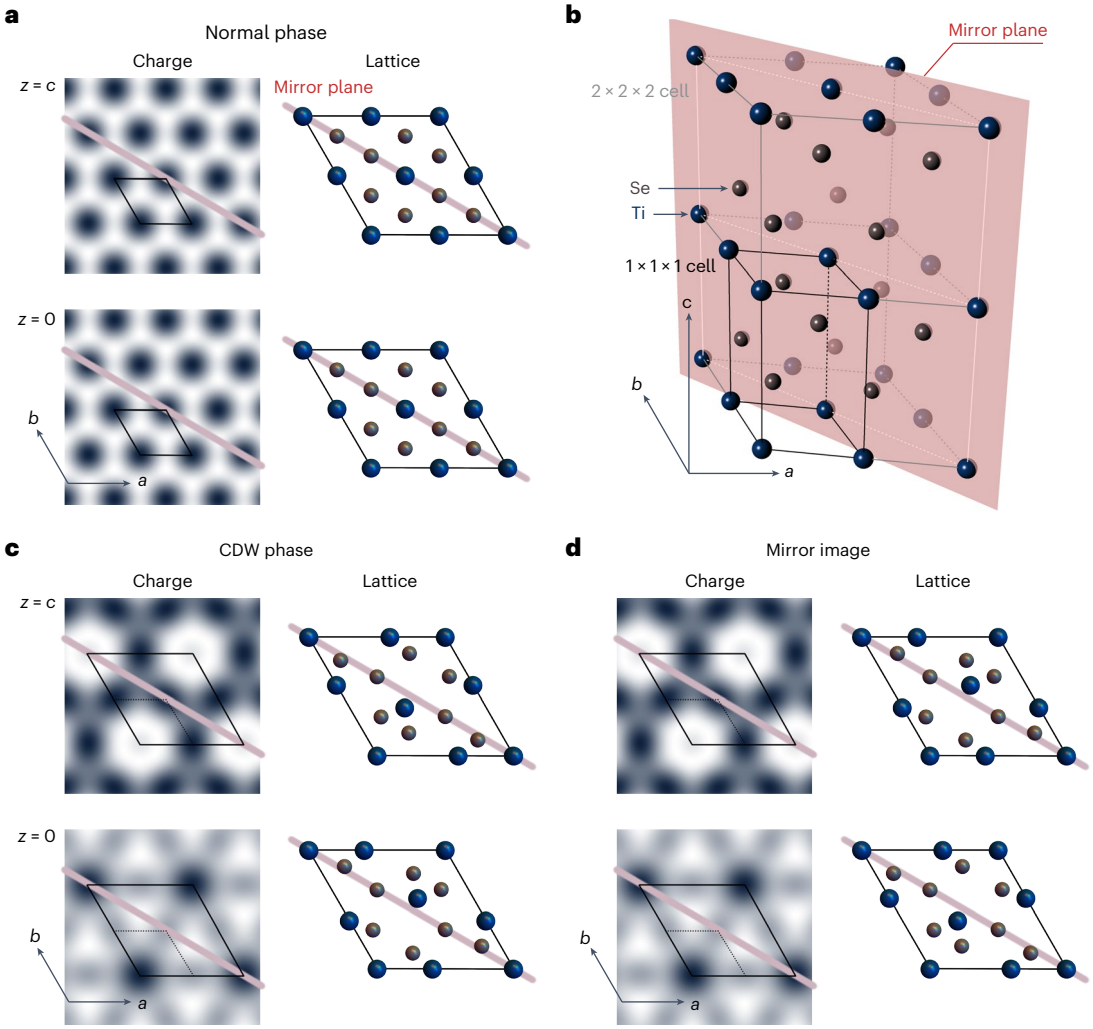

Fig. 1 | Charge-lattice symmetry frustration in 1T-$TiSe_2$. a,**c**, Charge density and atomic positions in the normal (**a**) and the CDW (**c**) phase, respectively. The 2 × 2 × 2 supercell is formed in the CDW phase. **b**, The lattice structure in the normal phase. The mirror plane is indicated by a red plane. **d**, The mirror image of the CDW phase. Whereas the charge density remain unchanged under the mirror reflection, one-half translation along the *c* axis is required to restore the lattice structure.

that the symmetry of any macroscopic property must include all symmetry elements of the lattice[20]. Is the lack of structure evidence merely due to our inability to resolve subtle lattice distortions even with modern synchrotron-based X-ray diffraction (XRD)? Or, does it signify possible violation of the fundamental principle and a profound flaw in our understanding of the structure-property relationship in quantum matters?

Although widely taken for granted, it is not trivial that ions on a discrete lattice are always able to precisely follow the symmetry of a continuous charge distribution of valence electrons, given the different transformation properties innate to scalar (charge) and vector (lattice) quantities. In this Article, we perform a rigorous symmetry analysis employing the full SG of 1T-$TiSe_2$. We show that the symmetry inconsistency is resolved by successive reduction of the symmetries of the two sectors until they become equivalent. In this process, all of the mirror, inversion and roto-inversion symmetries present in the system are lost. As a result, the system becomes chiral at the onset of the CDW, although neither the charge density modulation nor the atomic displacement is chiral by itself. We confirm this result by using inelastic X-ray scattering and Raman spectroscopy. We discuss implications of our result on the nature of chiral symmetry breaking phase transitions and possible violation of the Neumann's principle.

Charge-lattice symmetry frustration

Below the transition temperature $T_C \approx 200$ K, the triple-**q** CDW sets in with a 2 × 2 × 2 modulation of the charge density[21,22] (Fig. 1). The ordering wave vectors are $\mathbf{q}_{L_1} = (1/2, 0, 1/2)$, $\mathbf{q}_{L_2} = (0, -1/2, 1/2)$ and $\mathbf{q}_{L_3} = (-1/2, 1/2, 1/2)$, which connect the hole Fermi pocket centred at the zone centre (Γ) and the electron pockets at the three L points related by threefold rotation symmetry[23,24]. Concomitantly, lattice distortions result from condensation of *ab* plane polarized phonon modes of the same **q**'s (refs. 21,25–27) (Fig. 2).

The order parameters in the charge ($\delta\rho_L$) and the lattice ($\mathbf{d}_L^T$) sectors are written as

$$\delta\rho_L = \delta\rho_{L_1} + \delta\rho_{L_2} + \delta\rho_{L_3}, \tag{1}$$

$$\mathbf{d}_L^T = \mathbf{d}_{L_1}^T + \mathbf{d}_{L_2}^T + \mathbf{d}_{L_3}^T, \tag{2}$$

where

$$\delta\rho_{L_i} = \Re\, e^{i\mathbf{q}_{L_i}\cdot\mathbf{r}+\varphi_i}, \tag{3}$$

$$\mathbf{d}_{L_i}^T = \Re\, \boldsymbol{\epsilon}_i e^{i\mathbf{q}_{L_i}\cdot\mathbf{r}+\varphi_i}. \tag{4}$$

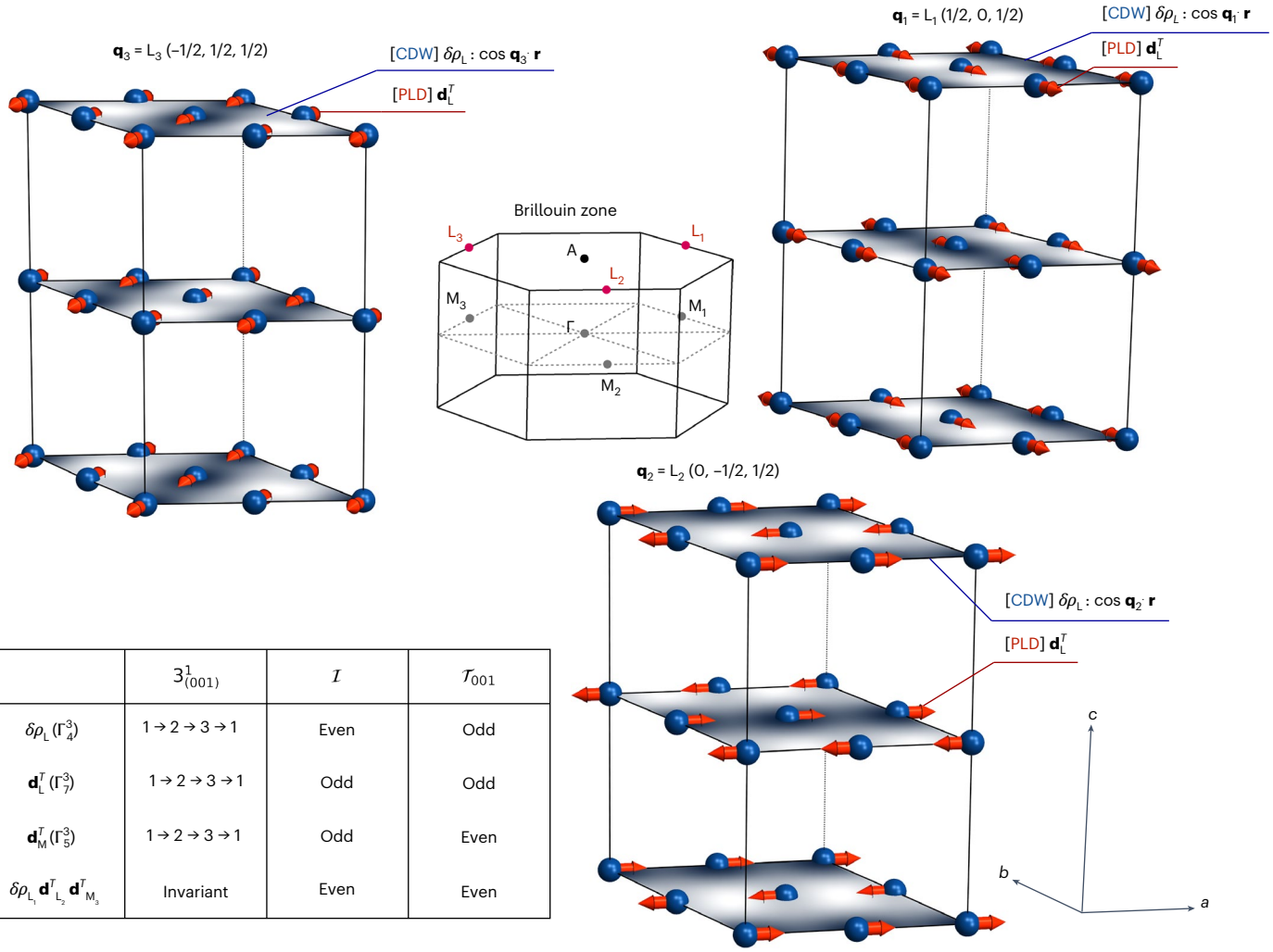

	$3^1_{(001)}$	$\mathcal{I}$	$\mathcal{T}_{001}$
$\delta\rho_L$ (Γ_4^3)	1 → 2 → 3 → 1	Even	Odd
$\mathbf{d}_L^T$ (Γ_7^3)	1 → 2 → 3 → 1	Odd	Odd
$\mathbf{d}_M^T$ (Γ_5^3)	1 → 2 → 3 → 1	Odd	Even
$\delta\rho_{L_1}\mathbf{d}^T{}_{L_2}\mathbf{d}^T{}_{M_3}$	Invariant	Even	Even

Fig. 2 | Transformation properties of CDWs and PLDs. $\delta\rho_{L_i}$ (CDW) and $\mathbf{d}_{L_i}^T$ (periodic lattice distortion (PLD)) are illustrated for each $\mathbf{q}_i$ (L$_1$, L$_2$ and L$_3$). The table lists the transformation properties $\delta\rho_{L_i}$ and $\mathbf{d}_{L_i}^T$ under the threefold rotation ($3^1_{(001)}$), inversion ($\mathcal{I}$) and unit translation along the c axis ($\mathcal{T}_{001}$). $\mathbf{d}_L^T$ ($\mathbf{d}_M^T$) has displacements out of phase (in phase) between adjacent layers. The initial phases φ_i are assumed to be zero. Only Ti atoms are shown for clarity.

Note that $\mathbf{d}_L^T$ has the same functional form as $\delta\rho_L$ apart from the polarization vector $\boldsymbol{\epsilon}_i$, which is transverse to $\mathbf{q}_i$ ($\boldsymbol{\epsilon}_i \cdot \mathbf{q}_i = 0$) (ref. 7). φ_i's give the initial phases for each component at the origin. Although most theoretical works assume this form of $\delta\rho_L$, we note that it is more convenient to express it in terms of symmetry-adapted harmonics, which we discuss in the 'Discussion' section.

One way in which a CDW acquires chirality is when the three components propagate out of phase with one another: that is, $\varphi_1 \neq \varphi_2 \neq \varphi_3$ (ref. 7). However, the chiral symmetry in the lattice sector cannot be broken with displacements as given by equation (4): it is straightforward to show that the lowest possible SG symmetry is $P\bar{1}$ (Supplementary Tables 1 and 23), which includes inversion and thus is always achiral regardless of φ_i values. In fact, the SGs are different even for the achiral CDW phase with $\varphi_1 = \varphi_2 = \varphi_3$. Upon inspection of the patterns of $\delta\rho_L$ and $\mathbf{d}_L^T$ shown in Fig. 1, it is clear that the mirror planes are replaced by glides by $\mathbf{d}_L^T$, changing the SG from $P\bar{3}m1$ to $P\bar{3}c1$, corresponding to the known high- and low-temperature structures, whereas they are preserved by $\delta\rho_L$. These considerations challenge the widespread notion that the charge and lattice sectors should have the same symmetry.

Symmetry analysis

We systematically check the symmetries preserved by $\delta\rho_L$ and $\mathbf{d}_L^T$. The symmetry elements in the symmorphic SG $P\bar{3}m1$ are generated by compounding a member R of the point group D_{3d} and a member T of the pure translation group $\mathcal{T}$, expressed as $\{R \mid T\}$. Because the order parameters are invariant under translations by twice the unit lattice vectors, it is sufficient to consider how they transform within the $2 \times 2 \times 2$ supercell. That is, from $\mathcal{T}$ we consider only the translation within the supercell given by $\{\mathcal{T}_{000}, \mathcal{T}_{100}, \mathcal{T}_{010}, \mathcal{T}_{110}, \mathcal{T}_{001}, \mathcal{T}_{101}, \mathcal{T}_{011}, \mathcal{T}_{111}\}$.

For simplicity, we assume here that $\varphi_1 = \varphi_2 = \varphi_3 = 0$, but this assumption is unnecessary in the full group-theoretical analysis provided in Supplementary Information sections 1 and 8. From Fig. 3, it is clear that $\delta\rho_L$ and $\mathbf{d}_L^T$ break different sets of symmetry elements. In particular, we note that the former (latter) is even (odd) under the space inversion about the origin (Fig. 2). Then, the symmetry of the system as a whole can only be as high as that of a group containing only the common symmetry elements preserved by both $\delta\rho_L$ and $\mathbf{d}_L^T$. They share only six symmetry elements, in which inversion, glide and roto-inversion symmetries are absent (Fig. 3). Thus, although neither $\delta\rho_L$ or $\mathbf{d}_L^T$ is chiral by itself, the system as a whole becomes chiral.

Accordingly, the lattice symmetry has to be lowered. The simultaneous presence of $\delta\rho_L$ and $\mathbf{d}_L^T$ induces lattice distortions that transform as the combined symmetry of $\delta\rho_L\,\mathbf{d}_L^T$. Although there are many such phonon modes, particularly important are the transverse phonon modes at the M point ($\mathbf{d}_M^T$), because these modes are also strongly coupled to CDW. Thus, allowed in the Landau free energy are terms that couple linearly to $\mathbf{d}_M^T$, of the form $\delta\rho_{L_1}\mathbf{d}_{L_2}^T\mathbf{d}_{M_3}^T$ plus its permutation of the indices, which always lower the free energy with non-zero $\mathbf{d}_M^T$

	$\mathcal{T}_{000}$	$\mathcal{T}_{100}$	$\mathcal{T}_{010}$	$\mathcal{T}_{110}$	$\mathcal{T}_{001}$	$\mathcal{T}_{101}$	$\mathcal{T}_{011}$	$\mathcal{T}_{111}$
E	CDW/PLD	-	-	-	-	-	-	-
$3^1_{(001)}$	CDW/PLD	-	-	-	-	-	-	-
$3^2_{(001)}$	CDW/PLD	-	-	-	-	-	-	-
$2_{(110)}$	CDW/PLD	-	-	-	-	-	-	-
$2_{(100)}$	CDW/PLD	-	-	-	-	-	-	-
$2_{(010)}$	CDW/PLD	-	-	-	-	-	-	-
$\mathcal{I}$	CDW	-	-	-	PLD	-	-	-
$\bar{3}^1_{(001)}$	CDW	-	-	-	PLD	-	-	-
$\bar{3}^2_{(001)}$	CDW	-	-	-	PLD	-	-	-
$\mathcal{M}_{(110)}$	CDW	-	-	-	PLD	-	-	-
$\mathcal{M}_{(100)}$	CDW	-	-	-	PLD	-	-	-
$\mathcal{M}_{(010)}$	CDW	-	-	-	PLD	-	-	-

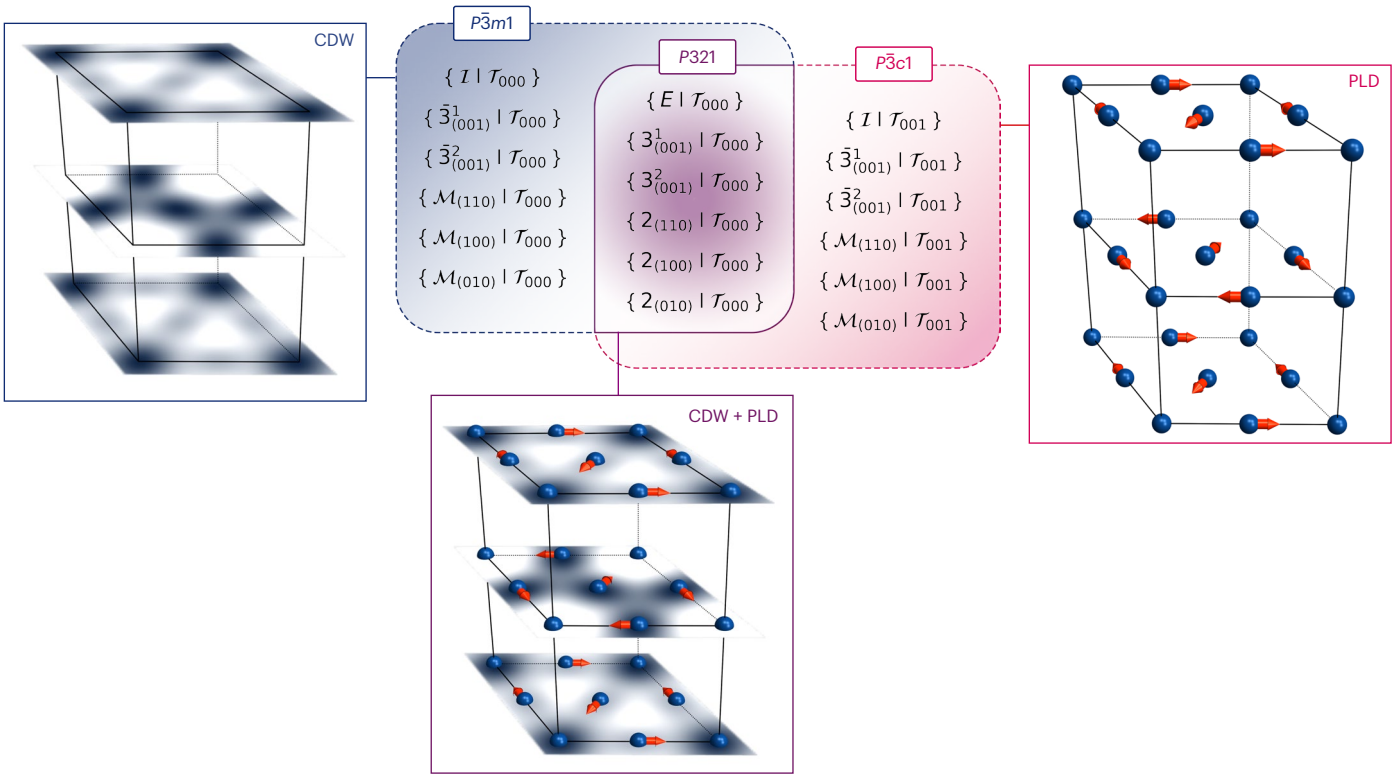

Fig. 3 | Space groups resulting from $\delta\rho_L$ and $\mathbf{d}^T_L$. An order invariant under translation by twice a unit vector along a, b and c axes is characterized by its transformation properties under symmetry operations $\{R \mid T\}$, where R is one of the members of the point group D_{3d} and T is one of the translations within the supercell. The symmetry operations preserved by $\delta\rho_L$ and $\mathbf{d}^T_L$ are written as CDW and PLD, respectively, in the table. CDW (PLD) leads to the SG $P\bar{3}m1$ ($P\bar{3}c1$) and their intersection to $P321$.

regardless of the sign of the coupling constant (Fig. 2 and Supplementary Fig. 1). With a non-zero $\mathbf{d}^T_M$, the highest symmetry SG is $P321$, which is further lowered to $P1$ when other induced displacements are considered (Supplementary Table 2). Indeed, our experimental data presented below are only consistent with $P2$ or $P1$.

Inelastic X-ray scattering

A verifiable prediction of our analysis is that there must be only one structural phase transition at $T_C \approx 200$ K, where the chiral symmetry breaks. In particular, we predict that there is no structural transition associated with condensation of the M phonon modes, despite being heavily renormalized by CDW fluctuations, as the transition is pre-empted by the induced $\mathbf{d}^T_M$. This is in contrast to the earlier predictions based on Landau theory, which predicts that the chiral CDW phase is reached on cooling through two phase transitions with the lower temperature one being at T^*[7,28]: (1) $\varphi_1 = \varphi_2 = \varphi_3$ for $T^* < T < T_C$, and (2) $\varphi_1 = 0$, $\varphi_2 = -\varphi_3 \neq 0$ for $T < T^*$, for which anomalies in transport and specific heat data suggest $T^* \approx 180$ K.

Figure 4a,b shows the inelastic X-ray scattering spectra along the high-symmetry lines L–A–Γ–M, measured at $T = 180$ K near T^*, in a transmission geometry sensitive to ab plane transverse L and M modes. Additional datasets collected at lower temperatures are presented in Extended Data Fig. 1. We measure only one of the three modes from L_1, L_2 and L_3 (and M_1, M_2 and M_3), because threefold rotation symmetry guarantees that their spectra are identical above T_C. Along A–L, a well-defined peak at ~4 meV at A disperses up in energy and bends down

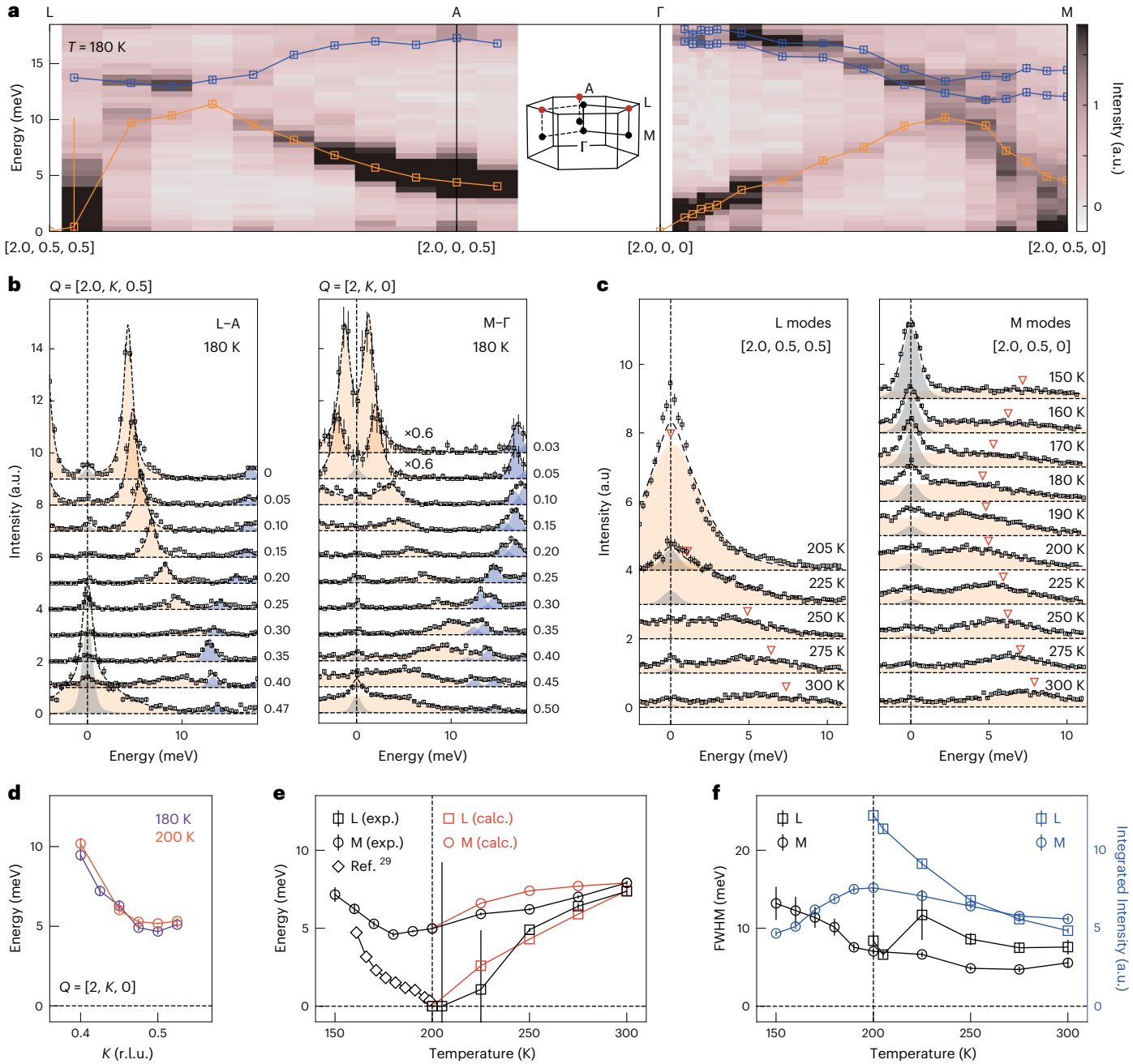

Fig. 4 | Comparison of L and M phonon modes softening. a, Phonon dispersion along L–A–Γ–M measured at $T = 180$ K. Orange and blue squares represent the peak centres of acoustic and optical modes, respectively, obtained by peak fitting. **b**, Spectra along L–A and M–Γ at 180 K. Orange and blue shaded regions are for acoustic and optical modes, respectively. **c**, Temperature dependence of the spectra at L and M. Orange triangles are the peak centres of the acoustic mode. **d**, Dispersions of the acoustic phonon at 180 K and 200 K near M. **e**, Temperature dependence of mode energies at L and M. Black markers (exp.) are obtained from measured data while orange markers (calc.) are derived from theoretical calculations. Diamond markers are phonon energies extracted from thermal diffuse scattering[26]. **f**, Black markers represent the temperature dependence of full-width-half maximum (FWHM). Blue markers represent integrated intensity of energy above 1 meV. Error bars indicate one standard deviation of Poisson statistic in **b**,**c** and one standard error of fitting parameters in **a**,**d**–**f**. All spectra are fitted with Lorentzian function with Bose factor. Wave vectors Q ([2, K, 0] or [2, K, 0.5] with K from 0.0 to 0.5) in **b**,**d** are given in reciprocal lattice units (r.l.u.).

as L is approached. The phonons are heavily damped near L, indicative of strong coupling to CDW fluctuations. A similar trend is found along Γ–M; the lineshapes become extremely broad as M is approached. At this temperature, L modes have already condensed, as is well established from earlier studies[26,27], but M modes remain at finite energies. Figure 4c–f shows the temperature evolution of L and M modes. At both L and M, elastic peaks appear below T_C, which are Bragg reflections associated with the formation of the supercell. Whereas L modes soften upon cooling, reaching zero energy at T_C from ~7 meV at room temperature, M modes remain at finite energies and harden below T^*. This can also be seen from the large increase of the integrated intensity (due to the Bose factor) observed for L modes when they condense, but not for M modes (Fig. 4f).

The similar behaviours of L and M modes are due to the quasi-two-dimensional nature of the electronic band structure, which expects similar amplitudes for Γ ↔ L and Γ ↔ M charge fluctuations,

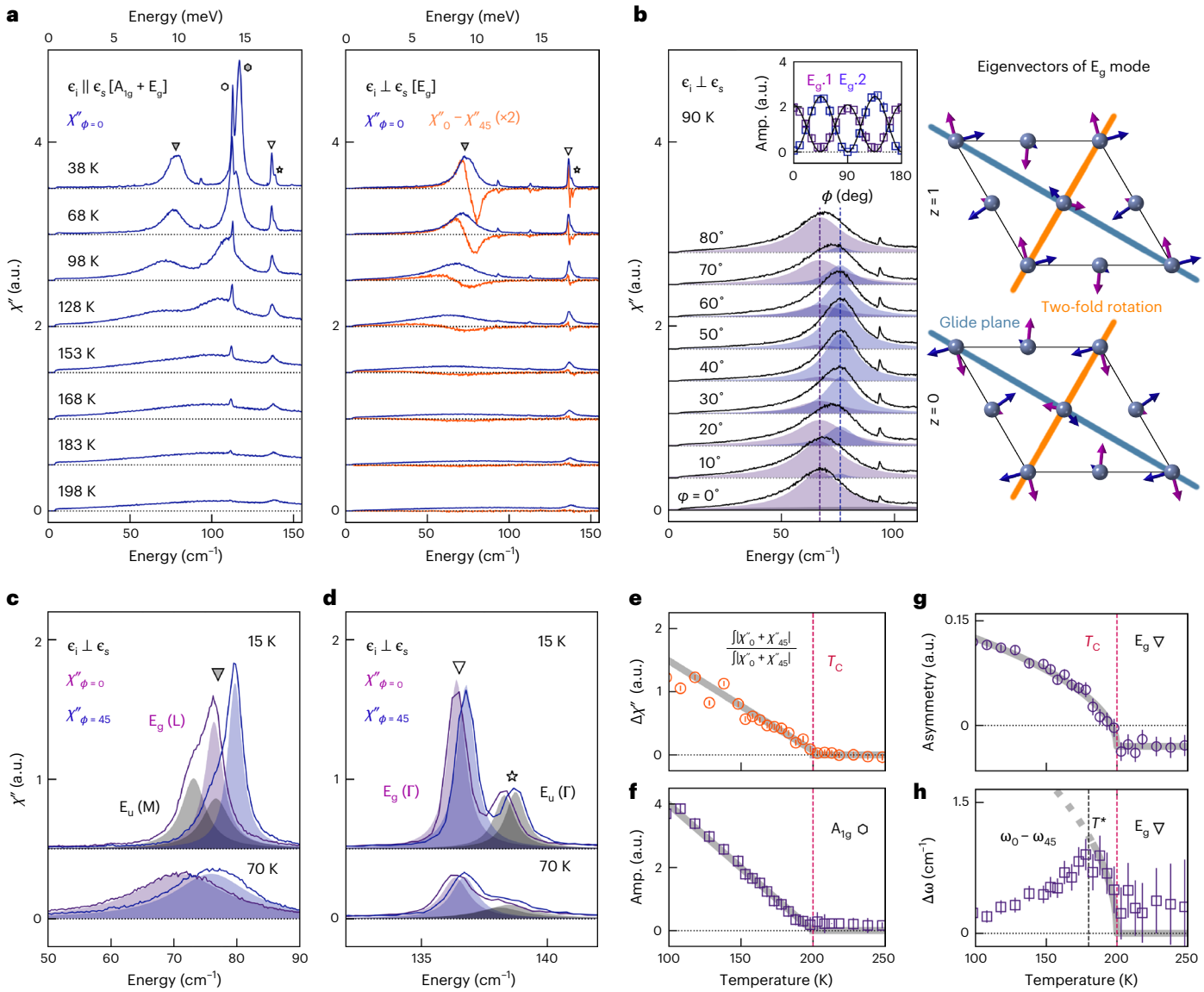

Fig. 5 | Chiral symmetry breaking. a, Temperature dependence of Raman spectra measured with parallel (left) and perpendicular (right) incident ($\boldsymbol{\epsilon}_i$) and scattered ($\boldsymbol{\epsilon}_s$) light polarizations. Hexagons, triangles and star indicate A_{1g}, E_g and E_u modes, respectively. Open markers are for zone-centre modes in the original unitcell, and closed ones are for zone-folded modes. Orange lines are differences between the spectra obtained at $\phi = 0°$ and at $\phi = 45°$. **b**, ϕ dependence of perpendicular spectra at $T = 90$ K. Dashed lines indicate the peak centres determined from $\phi = 0°$ and $\phi = 45°$ spectra. Inset displays the peak amplitudes, which are fitted (black lines) by the Raman tensor for C_{2h} point group. Eigenvectors for E_g modes are shown when they are degenerate. **c**,**d**, E_g and E_u modes at 15 K (**c**) and 70 K (**d**). **e**–**h**, Temperature dependence of the measure of splitting (**e**), zone-folded A_{1g} mode amplitude (amp.) (**f**), asymmetry of E_g mode at 135 cm^{-1} (**g**) and splitting of E_g mode at 135 cm^{-1} (**h**). Error bars indicate one standard error derived from fitting using Lorentzian and Fano functions, based on the least squares method.

renormalizing the phonon dispersions near L and M, respectively. Based on density-functional-theory and random-phase-approximation calculations, we reproduce the softening of L and M modes (Fig. 4a,e) using a three-parameter model (electron–hole exchange coupling, electron–phonon couplings for L and M modes) (details in Supplementary Information section 4). Our model takes into account the charge harmonics belonging to different irreducible representations, without which fitting to experimental data requires much larger coupling constants (Supplementary Figs. 4–9). Our central claim, however, only depends on the fact that there is no condensation of M modes at or below T_C, where our Raman data presented below show clear evidence for symmetry breaking below $P\bar{3}c1$. This can only be consistent with induced freezing of M modes, because a $2 \times 2 \times 2$ reconstruction can only involve L, A, Γ and/or M modes, and there are no anomalies at A and Γ (Supplementary Fig. 10).

Raman scattering

Because the Bragg peaks at L and M grow rapidly with decreasing temperature and dwarf inelastic signals, it is difficult to follow the phonon modes to low temperatures using inelastic X-ray scattering. Instead, they become visible in Raman spectra as they are back-folded into the zone centre. Using polarization-resolved Raman spectroscopy, we present direct evidence of chiral symmetry breaking at T_C. The point group of the SG is D_{3d} for both $P\bar{3}m1$ and $P\bar{3}c1$ SGs, which allows two species of Raman-active modes belonging to A_{1g} and E_g representations in the point group notation. Therefore, the threefold degenerate L and M modes split into a singlet and a doublet as they are back-folded. Their symmetries can be identified from the fact that A_{1g} (E_g) modes are allowed only when the incident and scattered photon polarizations are parallel to each other (visible in both parallel and cross polarization configurations) (Supplementary Fig. 2)[29].

First, we show that E_g doublets further split into singlets, which implies breaking of threefold rotation symmetry. Figure 5a shows the temperature dependence of Raman spectra. Slightly below T_C, the E_g doublet originating from back-folding of L modes are seen as a broad hump spanning energy range between 0 and 10 meV as in the inelastic X-ray scattering spectra. Upon cooling, it becomes a well-defined peak, although still much broader than other phonon modes, and hardens to ~75 cm^{-1}, consistent with the L mode identified in earlier Raman studies[30,31]. Figure 5b shows its polarization angle ($\phi = 0°$ when the incident photon is polarized along the a axis) dependence measured at $T = 90$ K. The peak centre shifts as ϕ is rotated, which means the doublet is split into two singlets (E_g. 1 and E_g. 2) that trade intensities with each other. Their intensities oscillate sinusoidally as a function of ϕ out of phase with each other, which is a behaviour expected for an E_g doublet. As they transform into each other by glide and twofold rotations (Fig. 5b), their splitting implies absence of these symmetries and that the symmetry of the lattice is lower than $P\bar{3}c1$. The highest SG symmetry consistent with this observation is $C2/c$; a necessary and sufficient condition for E_g mode splitting is breaking of threefold rotation symmetry, which implies breaking of at least one of the three glide planes (and also twofold rotations) related by the same symmetry.

Next, we determine the temperature at which the E_g mode splitting occurs. To this end, we plot in Fig. 5a the difference of the spectra measured at $\phi = 0°$ and $\phi = 45°$, where the intensity of one of the two modes becomes maximal and the other minimal. The difference spectrum clearly shows the splitting as a peak and a dip, and thus integrating its absolute value provides a measure for the symmetry breaking. From its temperature dependence plotted in Fig. 5e, it is clear that the onset of the splitting matches with T_C, which is independently measured by the intense A_{1g} mode appearing at ~120 cm^{-1} with zone folding (Fig. 5f). This result shows that the crystal structure with SG $P\bar{3}c1$, known as the low-temperature phase for more than four decades, is not realized at any temperature.

Upon a close inspection of the base temperature spectra shown in Fig. 5c, we also resolve M mode nearly degenerate with L mode. At $\phi = 0°$ and $\phi = 45°$, where one of the split doublets has vanishing intensity, we observe that the spectra still have asymmetric lineshapes, which can be well fitted with two peaks of similar widths having the same ϕ dependence. The M mode, however, has odd parity (Fig. 2), and thus its presence in the Raman spectra implies breaking of the inversion symmetry. This is further confirmed by the presence of infrared-active E_u mode at ~138 cm^{-1}, as shown in Fig. 5d (refs. 32,33). As the peak broadens at higher temperatures (Supplementary Fig. 3), it merges with a nearby E_g mode at ~135 cm^{-1}, a zone-centre mode in the original unit cell visible at all temperatures. Thus, fitting the spectra with a single peak with an asymmetric lineshape, we find that the asymmetry goes to zero at T_C (Fig. 5g), indicating inversion symmetry breaking at the onset of the CDW order. Thus, removing inversion symmetry from $C2/c$, SGs consistent with our Raman data are limited to $P1$, $P2$, $C2$ and Cc. Combined with the inelastic X-ray scattering result that $\mathbf{d}_M^T$ is induced at T_C, a possible low-temperature phase can only be either $P2$ or $P1$. $P2$ is further ruled out if we consider other phonon modes (not measured in this study) that must also be frozen (Supplementary Table 2).

Discussion

Our work comprehensively unravels the mechanism of chiral symmetry breaking in 1T-$TiSe_2$. Theoretically, provided that charge modulations and lattice distortions are given by equation (1) and equation (2) (Fig. 2), respectively, it follows that their simultaneous presence necessarily breaks chiral symmetry due to their different symmetry transformation properties (Fig. 3). Ever since the pioneering work by McMillan[34], equation (1) is assumed in all theoretical studies that we are aware of. But is it a priori obvious that the charge modulations can only be expressed as equation (1)? For example, if the phase transition is primarily driven by a lattice instability and charge modulations merely follow it, their spatial distributions would have the form of $\sin \mathbf{G} \cdot \mathbf{r} \cos \mathbf{q}_L \cdot \mathbf{r}$ where $\mathbf{G}_1 = 2(\mathbf{q}_{L_2} - \mathbf{q}_{L_3})$ (Supplementary Table 1). In other words, the lowest-order plane-wave components in the Fourier expansion of the charge modulations would be $\exp i(\mathbf{G} + \mathbf{q}_L) \cdot \mathbf{r}$ (Supplementary Fig. 12). However, this possibility is ruled out by the presence of superlattice peaks in the first Brillouin zone in the scanning tunnelling microscopy data[6,35].

With the rigorous group-theoretical analysis, the SG is uniquely determined to be $P1$. This is a highly unusual case where all but translation symmetries are broken at a second-order transition. A possible scenario is a phase transition driven by a chiral electronic instability, but this is unlikely considering the small density of states at the Fermi level. Instead, our work explains how the usual CDW instability, driven cooperatively by electron-lattice coupling[36,37], results in a chiral symmetry breaking without chiral instability in either the charge or the lattice sector. Further, our random-phase-approximation calculation starting from an effective field theory respecting $P\bar{3}m1$ SG symmetry reproduces the experimental data with reasonable parameters, which otherwise require much larger values to offset the weak Fermi surface nesting (Supplementary Figs. 4–9). More importantly, our formulation shows that the polarization bubble with generic momentum dependence can dynamically couple charge and lattice modes despite their different symmetries, which explains how two symmetry-distinct order parameters can arise at a single phase transition. This point is discussed in detail in Supplementary Information section 4.

Finally, we comment on the possible violation of Neumann's principle. Coming back to the earlier question: is the lattice always able to follow the symmetry of a charge modulation? In our case, the charge-lattice symmetry frustration is resolved through induced lattice distortions in the lowest-order coupling of $\delta\rho_L$, $\mathbf{d}_L^T$ and $\mathbf{d}_M^T$. However, it is not clear that phonon modes of an appropriate symmetry will generally be available in other systems. Formally, the frustration will eventually be resolved through higher-order couplings, but in our case the induced lattice distortions in the lowest order are already subtle enough to evade detection for many decades. Thus, in every practical sense, it may be possible to find a 'purely' electronic transition decoupled from the lattice if the symmetry mismatch is not resolved in the lowest order.

References

1. Asnin, V. M. et al. 'Circular' photogalvanic effect in optically active crystals. *Solid State Commun.* **30**, 565–570 (1979).
2. Taguchi, Y., Oohara, Y., Yoshizawa, H., Nagaosa, N. & Tokura, Y. Spin chirality, Berry phase, and anomalous Hall effect in a frustrated ferromagnet. *Science* **291**, 2573–2576 (2001).
3. Tokura, Y. & Nagaosa, N. Nonreciprocal responses from non-centrosymmetric quantum materials. *Nat. Commun.* **9**, 3740 (2018).
4. Son, D. T. & Spival, B. Z. Chiral anomaly and classical negative magnetoresistance of Weyl metals. *Phys. Rev. B* **88**, 104412 (2013).
5. Xiong, J. et al. Evidence for the chiral anomaly in the Dirac semimetal Na_3Bi. *Science* **350**, 413–416 (2015).
6. Ishioka, J. et al. Chiral charge-density waves. *Phys. Rev. Lett.* **105**, 176401 (2010).
7. van Wezel, J. Chirality and orbital order in charge density waves. *Europhys. Lett.* **96**, 67011 (2011).
8. Ishioka, J. et al. Charge-parity symmetry observed through Friedel oscillations in chiral charge-density waves. *Phys. Rev. B* **84**, 245125 (2011).

9. Pasztor, A. et al. Holographic imaging of the complex charge density wave order parameter. *Phys. Rev. Res.* **1**, 033114 (2019).
10. Yang, H. F. et al. Visualization of chiral electronic structure and anomalous optical response in a material with chiral charge density waves. *Phys. Rev. Lett.* **129**, 156401 (2022).
11. Singh, M. et al. Lattice-driven chiral charge density wave state in 1*T*-TaS_2. *Phys. Rev. B* **106**, L081407 (2022).
12. Jiang, Y.-X. et al. Unconventional chiral charge order in kagome superconductor KV_3Sb_5. *Nat. Mater.* **20**, 1353–1357 (2021).
13. Shumiya, N. et al. Intrinsic nature of chiral charge order in the kagome superconductor RbV_3Sb_5. *Phys. Rev. B* **104**, 035131 (2021).
14. Wang, Z. et al. Electronic nature of chiral charge order in the kagome superconductor CsV_3Sb_5. *Phys. Rev. B* **104**, 075148 (2021).
15. Fang, X.-Y., Hong, H., Chen, P. & Chiang, T.-C. X-ray study of the charge-density-wave transition in single-layer $TiSe_2$. *Phys. Rev. B* **95**, 201409(R) (2017).
16. Lin, M.-K., Hlevyack, J. A., Chen, P., Liu, R.-Y. & Chiang, T.-C. Comment on 'Chiral phase transition in charge ordered 1*T*-$TiSe_2$'. *Phys. Rev. Lett.* **122**, 229701 (2019).
17. Ueda, H. et al. Correlation between electronic and structural orders in 1*T*-$TiSe_2$. *Phys. Rev. Res.* **3**, L022003 (2021).
18. Zhang, R. et al. Second-harmonic generation in atomically thin 1*T*-$TiSe_2$ and its possible origin from charge density wave transitions. *Phys. Rev. B* **105**, 085409 (2022).
19. Xu, S.-Y. et al. Spontaneouos gyrotropic electronic order in a transition-metal dichalcogenide. *Nature* **578**, 545–549 (2020).
20. Orenstein, J. et al. Topology and symmetry of quantum materials via nonlinear optical responses. *Annu. Rev. Condens. Matter Phys.* **12**, 247–272 (2021).
21. Di Salvo, F. J., Moncton, D. E. & Waszczak, J. V. Electronic properties and superlattice formation in the semimetal $TiSe_2$. *Phys. Rev. B* **14**, 4321 (1976).
22. Woo, K. C. et al. Superlattice formation in titanium diselenide. *Phys. Rev. B* **14**, 3242 (1976).
23. Rossnagel, K., Kipp, L. & Skibowski, M. Charge-density-wave transition in 1*T*-$TiSe_2$: excitonic insulator versus band-type Jahn-Teller mechanism. *Phys. Rev. B* **65**, 235101 (2001).
24. Watson, M. D. et al. Orbital- and k_z-selective hybridization of Se 4*p* and Ti 3*d* states in the charge density wave phase of $TiSe_2$. *Phys. Rev. Lett.* **122**, 076404 (2019).
25. Bianco, R., Calandra, M. & Mauri, F. Electronic and vibrational properties of $TiSe_2$ in the charge-density-wave phase from first principles. *Phys. Rev. B* **92**, 094107 (2015).
26. Holt, M., Zschack, P., Hong, H., Chou, M. Y. & Chiang, T.-C. X-ray studies of phonon softening in $TiSe_2$. *Phys. Rev. Lett.* **86**, 3799 (2001).
27. Weber, F. et al. Electron-phonon coupling and the soft phonon mode in $TiSe_2$. *Phys. Rev. Lett.* **107**, 266401 (2011).
28. Castellan, J.-P. et al. Chiral phase transition in charge ordered 1*T*-$TiSe_2$. *Phys. Rev. Lett.* **110**, 196404 (2013).
29. Loudon, R. The Raman effect in crystals. *Adv. Phys.* **50**, 813–964 (2001).
30. Sugai, S., Murase, K., Uchida, S. & Tanaka, S. Raman studies of lattice dynamics in 1*T*-$TiSe_2$. *Solid State Commun.* **35**, 433–436 (1980).
31. Snow, C. S., Karpus, J. F., Cooper, S. L., Kidd, T. E. & Chiang, T.-C. Quantum melting of the charge-density-wave state in 1*T*-$TiSe_2$. *Phys. Rev. Lett.* **91**, 136402 (2003).
32. Subedi, A. Trigonal-to-monoclinic structural transition in $TiSe_2$ due to a combined condensation of q = (1/2, 0, 0) and (1/2, 0, 1/2) phonon instabilities. *Phys. Rev. Mater.* **6**, 014602 (2022).
33. Holy, J. A., Woo, K. C., Klein, M. V. & Brown, F. C. Raman and infrared studies of superlattice formation in $TiSe_2$. *Phys. Rev. B* **16**, 3628 (1977).
34. McMillan, W. L. Landau theory of charge-density waves in transition-metal dichalcogenides. *Phys. Rev. B* **12**, 0087 (1975).
35. Hildebrand, B. et al. Local real-space view of the achiral 1*T*-$TiSe_2$ 2 × 2 × 2 charge density wave. *Phys. Rev. B* **120**, 136404 (2018).
36. van Wezel, J., Nahai-Williamson, P. & Saxena, S. S. Exciton-phonon-driven charge density wave in $TiSe_2$. *Phys. Rev. B* **81**, 165109 (2010).
37. Zenker, B., Fehske, H., Beck, H., Monney, C. & Bishop, A. R. Chiral charge order in 1*T*-$TiSe_2$: Importance of lattice degrees of freedom. *Phys. Rev. B* **88**, 075138 (2013).

Methods

1T-$TiSe_2$ crystals

1T-$TiSe_2$ single crystals grown by chemical vapour transport technique were purchased from HQ Graphene. All samples used in this study were prepared from the same single crystal.

Inelastic X-ray scattering

High-resolution inelastic X-ray scattering experiment was carried out at the 30-IR HERIX beamline of the Advanced Photon Source. The total energy resolution was about 1.5 meV at the incident energy of 23.71 keV using Si (12, 12, 12) reflection of the monochromator. A sample of 50 µm thickness was mounted on a closed-cycle cryostat and measured in a transmission geometry. Spectra were obtained along high-symmetry lines L–A–Γ–M, which, respectively, correspond to $\mathbf{q}$ = (2, 1/2, 1/2), (2, 0, 1/2), (2, 0, 0) and (2, 1/2, 0). The Lorentzian function with Bose factor was used for fitting:

$$I(\omega) = \frac{A}{1-e^{-\omega/k_BT}} \times \left(-\frac{\Gamma/2}{(\omega+\omega_0)^2+(\Gamma/2)^2} + \frac{\Gamma/2}{(\omega-\omega_0)^2+(\Gamma/2)^2}\right), \quad (5)$$

where Γ is the full-width at half-maximum. Γ and ω_0 are shown as black markers in Fig. 2e,f, respectively.

An additional inelastic X-ray scattering experiment was performed at the BL35XU beamline of the SPring-8 (ref. 38). The incident X-ray energy was 21.747 keV with energy resolution of 1.6 meV. Phonon dispersion spectra were obtained for temperatures 6 K and 100 K (below T^*) along high-symmetry lines L–A–Γ–M. Also, the temperature dependence of the acoustic mode at the M point was measured over an extended range (Extended Data Fig. 1).

Raman spectroscopy

Raman spectroscopy was performed on a home-built instrument equipped with 750 mm spectrometer and liquid-nitrogen-cooled charge-coupled-device detector using a 633 nm laser as an excitation source. Bragg grating notch filters were used to suppress elastic signals, allowing measurement of inelastic signals above 5 cm^{-1} with a resolution of 0.33 cm^{-1}. Parallel (∥) and crossed (⊥) polarizations of the incident and scattered lights propagating along the *c* axis were measured in a back-scattering geometry. The incident light polarization was rotated about the *c* axis using half-wave plates. The laser power and beam-spot size are kept below 0.5 mW and 2 µm, respectively, which gave laser heating of 10 K estimated based on the Stokes and anti-Stokes intensity ratio.

XRD

Prior to inelastic X-ray scattering measurements, samples were tested for consistency with earlier works using XRD. An XRD series on a representative 1T-$TiSe_2$ sample prepared from the same single crystal was collected on a STOE imaging plate diffraction system (IPDS-2T) using Mo K_α radiation. For the investigated specimen, all accessible reflections (~21,000) were measured up to a maximum angle of 2Θ = 65°. The data were corrected for Lorentz, polarization, extinction and absorption effects. Using SHELX[39] and JANA2006 (ref. 40), all averaged symmetry-independent reflections ($I > 2\sigma$) have been included for the refinements. For all temperatures, the unit cell and the SG were determined, the atoms were localized in the unit cell utilizing random phases as well as Patterson superposition methods, the structure was completed and solved using difference Fourier analysis, and finally the structure was refined. In all cases, the refinements converged quite well and showed excellent reliability factors (see GOF, R_1 and wR_2 in Supplementary Table 5).

Additional XRD experiments were performed at the 1C beamline of the Pohang Light Source using reflection geometry with an incident energy of 11.216 keV to search for weak forbidden reflections. To reduce the background, a Si (8, 4, 4) bent analyser was positioned between the sample and the detector, which gave a signal-to-noise ratio better than 10^7 (ref. 41).

Data availability

All data that support the conclusions of this work are available from the corresponding author upon reasonable request.

References

38. Baron, A. Q. R. et al. An x-ray scattering beamline for studying dynamics. *J. Phys. Chem. Solids* **61**, 461 (2000).
39. Sheldrick, G. M. A short history of SHELX. *Acta Crystallogr. A* **64**, 112–122 (2008).
40. Petrícek, V., Dušek, M. & Palatinus, L. Crystallographic computing system JANA2006: general features. *Z. Kristallogr. Cryst. Mater.* **229**, 345–352 (2014).
41. Kim, J.-K. et al. Resonant inelastic x-ray scattering endstation at the 1C beamline of Pohang Light Source II. *J. Synchrotron Radiat.* **30**, 643–649 (2023).

Acknowledgements

We thank J. van Wezel and A. Subedi for insightful discussions. This project is supported by IBS-R014-A2 and National Research Foundation (NRF) of Korea through the SRC (grant no. 2018R1A5A6075964). The use of the Advanced Photon Source at the Argonne National Laboratory was supported by the U.S. Department of Energy under contract no. DE-AC02-06CH11357. The additional synchrotron radiation experiments were performed at BL35XU of SPring-8 with the approval of the Japan Synchrotron Radiation Research Institute (proposal no. 2023B1728). C.K. acknowledges support by the Institute for Basic Science in Korea (grant nos. IBS-R009-G2, IBS-R009-D1) and a NRF of Korea grant funded by the Korea government (MSIT) (grant no. 2022R1A3B1077234). J.M.B. acknowledges support by the NRF of Korea (grant no. 2022R1C1C2008671). K.-S.K. is supported by the Ministry of Education, Science and Technology (grant no. RS-2024-00337134) of the NRF of Korea and by the TJ Park Science Fellowship of the POSCO TH Park Foundation.

Author contributions

B.J.K. conceived and managed the project. H.-W.J.K., K.K., D.I., T.M., H.F., A.Q.R.B., A.A. and A.S. performed inelastic X-ray scattering experiments. K.K. and H.K. performed Raman scattering experiments. S.H., K.K., J.-K.K., J. Kim and J. Kwon performed synchrotron-based XRD experiments. H.K., J.S., S.J. and C.K. performed second harmonic generation experiments. M.M. and M.L.T performed structure refinement using XRD. K.K., H.-W.J.K., S.H. and B.J.K. performed representation analysis. J.M.B. and K.-S.K. performed random-phase-approximation calculations. K.K., H.-W.J.K., S.H., J.M.B., K.-S.K. and B.J.K. wrote the paper with input from all authors.

Competing interests

The authors declare no competing interests.

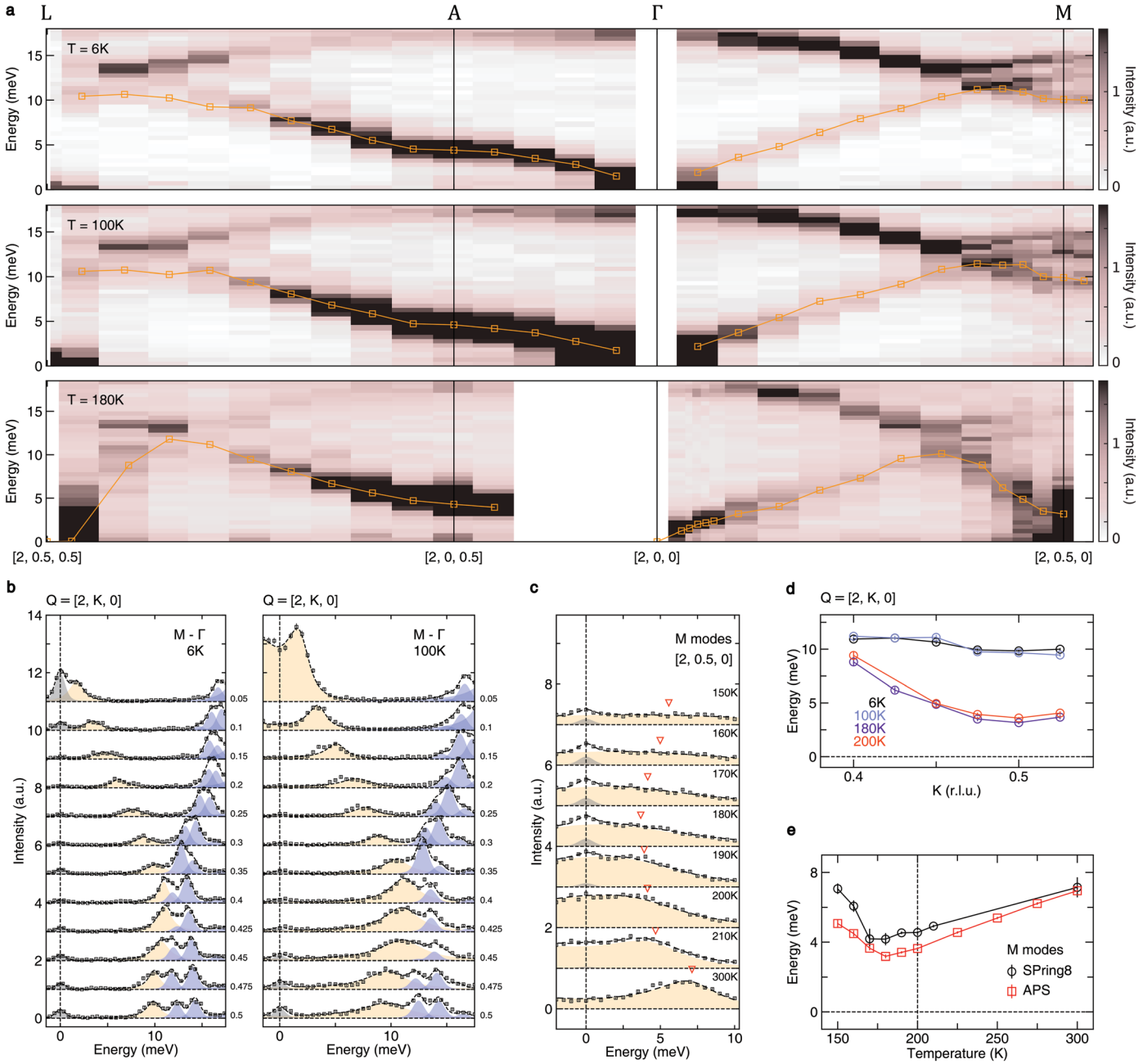

Extended Data Fig. 1 | Additional inelastic x-ray scattering spectrum at 6 K and 100 K. a, Phonon dispersion along L – A – Γ – M measured at 6 K (above), 100 K (middle) and 180 K (below), respectively. Orange line represents the peak centre of the acoustic phonon mode. **b**, Spectrum along M – Γ at 6 K (left) and 100 K (right). Orange and blue shaded regions represent acoustic and optical phonon modes, respectively. **c**, Temperature dependent spectra at M point. Red triangles indicate the peak centre of the acoustic mode. **d**, Acoustic phonon dispersion near M point at 6 K, 100 K, 180 K and 200 K. **e**, Temperature dependence of acoustic mode energy. Error bars indicate one standard deviations of Poisson statistic in **b**, **c** and one standard errors on the fitting parameters in **a**, **e**, **d**. All spectra are fitted with Lorentzian function with Bose factor.